frontiers | Frontiers in Marine Science

TYPE Original Research
PUBLISHED 18 November 2025
DOI 10.3389/fmars.2025.1717972

OPEN ACCESS

EDITED BY
Eun Young Lee,
University of Vienna, Austria

REVIEWED BY
Ildiko Gyollai,
Konkoly Observatory (MTA), Hungary
Hengchao Xu,
Chinese Academy of Sciences (CAS), China

*CORRESPONDENCE
Natalia Shulga
nash.ocean@gmail.com

RECEIVED 03 October 2025
ACCEPTED 29 October 2025
PUBLISHED 18 November 2025

CITATION
Shulga N, Perfilov P and Ryazantsev K (2025) Integrated geochemical and biomarker signature of fast-growing Fe-Mn nodules from the Gulf of Finland, Baltic Sea. *Front. Mar. Sci.* 12:1717972. doi: 10.3389/fmars.2025.1717972

Integrated geochemical and biomarker signature of fast-growing Fe-Mn nodules from the Gulf of Finland, Baltic Sea

Natalia Shulga[1]*, Peter Perfilov[1] and Konstantin Ryazantsev[2]

[1]Shirshov Institute of Oceanology, Russian Academy of Sciences, Moscow, Russia, [2]Vernadsky Institute of Geochemistry and Analytical Chemistry, Russian Academy of Sciences, Moscow, Russia

Ferromanganese (Fe-Mn) nodules, characterized by rapid growth and diverse morphologies, are widespread on the Baltic Sea seafloor. This study provides a comprehensive analysis of the bulk elemental composition, internal structures, and organic matter (OM) characteristics based on n-alkane distributions in Fe-Mn nodules and their underlying sediments from the Gulf of Finland. The investigated nodules are of diagenetic origin and include both Fe-rich and Mn-rich types. The have spheroidal and discoidal morphologies with pronounced concentric layering. The results indicate that the nodules accumulate both terrestrial and bacterially derived OM which undergoes active diagenetic transformation. Regularized Canonical Correlation Analysis (rCCA) applied to this integrated dataset revealed a strong multivariate relationship between organic matter and elemental composition. The analysis of Internal microstructures revealed microglobular, twisted fibrous, and colloform textures, alongside biomorphic features. These textures reflect coupled abiotic and biological mineralization processes. The absence of correlation between nodule morphology, geochemical type, and underlying sediment properties demonstrates that highly localized microenvironments control nodule formation. This study refines the genetic model of shallow-water fast-growing Fe-Mn nodules, highlighting the crucial role of organic matter-driven diagenesis under dynamic redox conditions in ore formation.

KEYWORDS

diagenesis, Geochemistry, n-alkanes, rCCA, redox conditions

1 Introduction

Ferromanganese (Fe-Mn) nodules are widespread on the Baltic Sea floor, particularly in the Gulf of Finland. Their formation and growth occur at high rates (0.014-0.028 mm/yr) (Grigoriev et al., 2013) within a complex system governed by hydrodynamic, physico-chemical, diagenetic, and microbiological processes (Glasby et al., 1997; Kuhn et al., 2017). The unique oceanographic setting of the Baltic Sea, characterized by estuarine circulation, stable water column stratification, high primary productivity, and regional eutrophication

(Vallius, 2007), creates a dynamic redox environment that is crucial for shallow-water nodules genesis. Various geochemical and mineralogical aspects of Fe-Mn nodules in the Gulf of Finland have been described in previous studies (Zhamoida et al., 1996, Zhamoida et al., 2007; Glasby et al., 1997; Zhang et al., 2002; Baturin, 2009; Wang et al., 2010; Wasiljeff et al., 2024).

In addition to the well-established diagenetic model, a biogeochemical hypothesis for nodules formation is gaining support, emphasizing the role of microbial processes (Ehrlich, 1999; Wang et al., 2012; Tully and Heidelberg, 2013; Yli-Hemminki et al., 2014; Blöthe et al., 2015; Shi et al., 2016; Shiraishi et al., 2016; Shulse et al., 2017; Lindh et al., 2017; Jiang et al., 2020; Molari et al., 2020; Shulga et al., 2022; Lai et al., 2024; Majamäki et al., 2025). As key agents of diagenesis, microorganisms directly influence iron and manganese cycling through oxidation of Fe^{2+} and Mn^{2+} for energy, and reduction of Fe^{3+} and Mn^{4+} as terminal electron acceptors in respiratory chains.

However, critical gaps remain in understanding organic matter (OM) cycling within these shallow-water nodules. Specifically, pathways of OM incorporation and its subsequent diagenetic transformation are poorly constrained, with no dedicated studies on this subject in the Baltic Sea region. Furthermore, a significant challenge in comparative nodules research lies in dataset heterogeneity. Geochemical, mineralogical, and microbiological data are often obtained from different sample sets collected under varying conditions, or reported only as averaged values and concentration ranges. This practice limits robust statistical analysis and obscures individual geochemical signatures essential for understanding microenvironmental controls during nodules formation.

This study presents the first comprehensive investigation of morphologically diverse Fe-Mn nodules from the Gulf of Finland using an integrated approach. We simultaneously analyze both inorganic (bulk elemental composition) and organic (n-alkane distributions) constituents within the same individual samples, alongside characteristics of the underlying sediments. The primary objectives are to: (1) determine the geochemical composition of nodules and underlying sediments; (2) characterize sources and diagenetic transformation of organic matter within nodules; (3) identify relationships between geochemical and organic parameters using multivariate statistics. By providing a coherent dataset from individually analyzed samples, this work aims to refine genetic models for shallow-water Fe-Mn nodules and establish a robust foundation for future comparative studies.

2 Materials and methods

2.1 Study area

The Baltic Sea is one of the world's largest brackish-water inland seas, with a surface area of 419,000 km² (Vallius, 2007). This shallow basin (average depth ~50 m), coupled with a vast catchment area (1.641 million km²), creates conditions leading to high sedimentation rates, reaching 1–6 m/kyr. This allows the Baltic Sea sediments to act as a high-resolution archive, offering a detailed chronology of environmental and climatic shifts over the post-glacial period. The Gulf of Finland is shallow, with an average depth of 38 m and a maximum depth of 121 m. The hydrological regime of the gulf is dominated by the Neva River, which has an annual runoff of 83.5 km³ (Vallius, 2007). The seafloor topography of the Gulf of Finland is characterized by numerous semi-isolated basins, islands, and elevations.

2.2 Sampling

Fe-Mn nodules and underlying sediments were collected during the research cruise ACB51 in 2021 from the Gulf of Finland, Baltic Sea (Figure 1). Sampling was performed using a Van Veen grab sampler. The coordinates and water depths of the sampling sites are listed in Table 1. A visual lithological description of the sediments was performed directly in the grab sampler. At each site, the dominant nodule type was identified based on size and morphology. Representative nodules of this dominant type were carefully retrieved from the grab with sterile tweezers, gently rinsed with ambient seawater to remove loose sediment, placed in sterile zip-lock bags, and immediately frozen at -21 °C. The samples were maintained at this temperature during transport to the laboratory. The underlying sediments were subsampled to specifically target the upper oxidized layer and the underlying reduced layer, reflecting the redox boundary at which Fe-Mn nodule growth occurs. Sediments were collected from the same grabs using a pre-sterilized stainless-steel spatula, stored in zip-lock bags, and preserved under the same freezing conditions as the nodules. While the collected samples were intended for a broader multidisciplinary analysis, this study focuses exclusively on the geochemical composition and organic matter characteristics (n-alkanes) of the nodules. The results of concomitant microbiological (genetic) analyses and detailed lipid biomarker profiling (fatty acids, sterols) will be presented in forthcoming publications.

2.3 Fe-Mn nodules and underlying sediments analyses

2.3.1 Geochemistry

The bulk nodules (58 samples), their different parts and underlying sediments (13 samples) were freeze-dried, ground, homogenized, and analyzed for the content of major and some trace elements (Na, Mg, P, S, K, Ca, Al, Ti, V, Cr, Mn, Fe, Co, Ni, Cu, Zn, and Sr) by ICP atomic emission spectrometry (ICP-AES) (ICAP-61, Thermo Jarrell Ash, USA). The trace-element (Li, Sc, Cr, Ni, Cu, Zn, Sr, Mo, Cd, Ba, W, and Pb) concentrations of the samples listed above were determined by ICP-MS (X-7, Thermo Elemental, USA). Samples were dried, crushed to powder size and dissolved with HNO_3 + H_2O_2 (4:1 by volume, Merck) in an autoclave system. The accuracy of the measurements was 3-5%. Analytical precision and accuracy were checked by analyses of

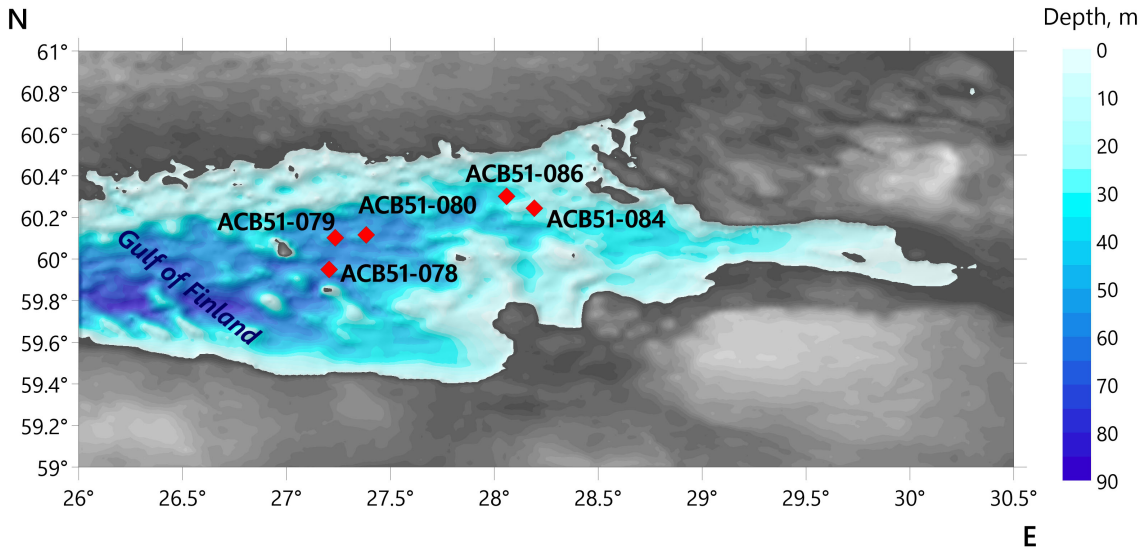

FIGURE 1
Bathymetric map of the Gulf of Finland (Baltic Sea) with indication of sampling sites (red dots).

standards OCO-408-10-1, OCO-408-10–2 and AGV-2 (Supplementary Table S2). A detailed description of the methodology and accuracy is given in Karandashev et al (Karandashev et al., 2008).

2.3.2 Scanning electron microscopy

Prior to thin-section preparation, the nodules were stabilized by vacuum impregnation using a low-viscosity epoxy resin to ensure structural integrity during cutting. The most representative areas, up to 25×45 mm, were selected and then thin sections (about 200 µm thick) were made for SEM investigation. Backscattered electron (BSE) imaging, secondary electron (SE) imaging and energy dispersive X-ray spectroscopy (EDS) analyses were performed using Tescan scanning electron microscope Mira 3 with analytical equipment of the Oxford Instruments AztecLive Automate with detector Max 80. The SEM was operated at 10 kV for BSE images, 4 kV for SE images and 20 kV for EDS analyses. Sections were subsequently mapped in Mn, Fe and Si X-rays using the Aztec program. Mn, Fe and Si were measured using Kα lines. Investigations of the nodule microstructures were made by SEM analyses with a Mira 3 TESCAN. Polished thin, 150 µm-thick sections were prepared. Fragments of the inner parts of nodules were selected for the identification of microstructures and textures. The surface of the samples was covered with 15 nm-thick gold with Balzers SCD 030 equipment. Major element concentrations were determined using energy-dispersive X-ray spectroscopy on an X-MAX 80 (EDS, Oxford Instruments, UK). Analyses were conducted at 20 kV using a diaphragm of 60 µm. Data analysis was carried out using the INCA Oxford software package.

2.3.3 Grain size

Distribution in underlying sediments (13 samples) was studied on a SHIMADZU SALD 2300 laser diffraction grain size analyzer. Preparation of bulk samples for grain size analysis (1–2 g sample) included keeping the sample for 24 h in distilled water (20 mL) with the addition of 20 mL of sodium hexametaphosphate solution (0.7% $Na_6P_6O_{18}$). Immediately before analysis, the sample beaker was placed in an ultrasonic bath for 5 min to disperse the particles. In the analyzer, the sample was exposed to ultrasound for 1 min. The average size of sediment particles was calculated according to the method in (Folk and Ward, 1957).

2.3.4 Bulk analyses

The freeze-dried nodule and sediment samples were ground in a mortar. Total organic carbon (TOC) was measured on a Shimadzu L-VPH. TOC was determined on decalcified (acidification with 10% HCl) samples. The instrument was calibrated using standards SDO-2 for sediments and SDO-4 for nodules (Potts et al., 1992).

2.3.5 GC–MS

For the n-alkane analyses, the nodule and sediment samples were stored at -21°C directly after collecting. The freeze-dried samples (10–20 g) were ground, homogenized, and subjected to extraction under ultrasonication with dichloromethane:methanol mixture (9:1). The total extract was purified from sulfur using activated copper. The n-alkanes were separated from the other fractions by liquid chromatography on silica gel with hexane as the eluent. GC–MS analyses were performed using a Shimadzu-TQ8040 using a Rxi-5Sil MS 30 m × 0.25 mm × 0.25 µm capillary column (RESTEK). The temperature program was as follows: starting with 3 min at 60°C, then heating to 300°C at 4°C/min, and then holding 30 min at 300°C. The injection volume was 2 µl, splitless. Carrier gas was helium with a flow rate of 1.5 ml/min. The analysis was made as a total scan from m/z 50 to 650 (70 eV). Identification and quantification of n-alkanes and isoprenoids (pristine Pr, phytane Ph) were made on the basis of the retention times of the calibration mixture (n-C_8-C_{20}, n-C_{21}-C_{40}

TABLE 1 Location of sampling sites in the Gulf of Finland, Baltic Sea.

Sampling Site	Latitude, N	Longitude, E	Depth, m
ACB51-078	59°56.9346'	27°12.3589'	62
ACB51-079	60°06.1474'	27°14.1052'	55.2
ACB51-080	60°06.9864'	27°22.9793'	54
ACB51-084	60°14.6879'	28°11.5248'	24
ACB51-086	60°18.0754'	28°03.6084'	33

mixtures, Supelco) and NIST mass-spectral library. Response factors were determined relative to squalane (2,6,10,15,19,23-hexamethyltetracosane) as the internal standard. Concentrations of individual hydrocarbons were reported in μg/g of the dry sample.

2.3.6 Statistical analysis

To explore the multivariate relationships between the elemental composition and the n-alkane biomarker content, a regularized canonical correlation analysis (rCCA) was employed. This method was selected because it is specifically designed to identify the shared structure between two sets of variables, without imposing a cause-and-effect framework. Unlike Principal Component Analysis (PCA), which reduces a single dataset, or Redundancy Analysis (RDA), which models a response matrix as a function of predictors, CCA symmetrically finds pairs of patterns from each dataset that are maximally correlated. This approach was optimal for our goal of understanding the integrated relationship between the inorganic and organic geochemical data. The regularized extension (rCCA) was necessary to prevent overfitting, given that the number of variables exceeded the number of samples (Borcard et al., 2018; Uurtio et al., 2018). All variables were standardized using z-score normalization prior to analysis (Supplementary Tables S3, Supplementary Tables S4). The statistical significance of the canonical correlations was assessed using Bartlett's sequential test, and a correlation threshold of $|r| > 0.6$ was applied to the canonical biplot to highlight the most influential variables (Bartlett, 1941). All computations were performed in R (v4.4.0) using the mixOmics package (Team, 2019).

3 Results

3.1 Morphological type

According to the established classification for the Baltic Sea (Zhamoida et al., 1996), three main morphological types of Fe-Mn deposits are recognized: spheroidal nodules, discoidal nodules, and crusts. This study focuses on the analysis of the first two morphological types, collected at five sites in the Gulf of Finland (Figure 2).

Site ACB51-078. Discoidal Fe-Mn nodules, ranging in size from 15×10×6 mm to 120×70×10 mm. They exhibit a flattened morphology, commonly with rock fragments as nuclei. The upper surface is smooth and has an ochre color, while the lower surface is rough and ranges from brown to black.

Site ACB51-079. Discoidal Fe-Mn nodules, ranging in size from 35×30×7 mm to 120×90×12 mm. They are characterized by a flat,

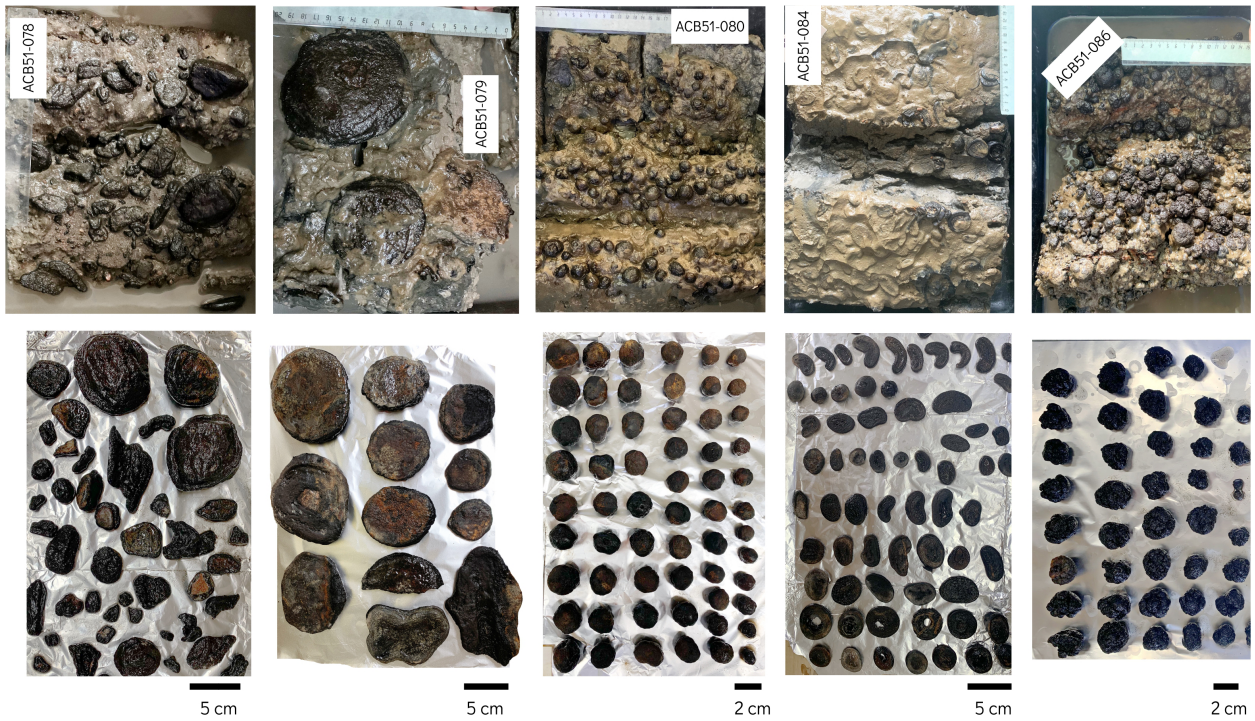

FIGURE 2
Photos of Fe-Mn nodules collected at sampling sites in the Gulf of Finland. The location of sampling sites is shown in Figure 1.

rounded shape with rock fragment nuclei. The upper surface is smooth and ochre-colored, whereas the lower surface is rough and brown to black. A sub-type of irregularly shaped flat nodules was also identified. These have a smooth surface, with color varying from grey-black to ochre. Based on size, the nodules are clearly distinguished as small (S), medium (M), and large (L).

Site ACB51-080. Spheroidal Fe-Mn nodules, 9 to 13 mm in diameter. The nuclei consist primarily of clayey material. The surface is black and non-uniform in color, and smooth. The internal structure is layered.

Site ACB51-084. Discoidal, so-called "penny-shaped" nodules; 1–3 cm in diameter and 0.3-0.4 mm thick. The surface is smooth. The nuclei consist of sediment or rock fragments, around which distinct layers of Fe-Mn oxyhydroxides are clearly visible. The surfaces are ochre in color.

Site ACB51-086. Spheroidal nodules; ranging from 3 mm (micronodules) to 15 mm in diameter. The surface texture is smooth (SG) and/or botryoidal (SE). The nuclei are composed of dense ore mass. The transition zone from the nucleus to the surface is impregnated with sedimentary material, and the outer crust is dense and layered. The surfaces are saturated black.

3.2 Internal structure

Backscattered electron (BSE) imaging of thin sections reveals distinct growth structures in the studied nodules. The spheroidal, Fe-rich nodule (ACB51-080) exhibits well-defined concentric zonality, whereas the discoidal, Mn-rich nodule (ACB51-079) is characterized by an asymmetric, laterally-persistent layering (Figures 3, 4). This zonality is expressed by a rhythmic alternation of dark, low-reflectivity (Mn-rich) layers and bright, highly-reflective (Fe-rich) layers, as confirmed by elemental mapping. The internal structure of the spheroidal nodule is dense and compact, with layers forming continuous, closed rings around a central nucleus. In contrast, the discoidal nodule displays a more complex texture. Its asymmetry is defined by a significant thickening of the Fe-Mn layers on one side, suggesting preferential growth oriented towards the sediment-water interface. Furthermore, the layers in the discoidal nodule are less continuous and exhibit greater micro-scale variation in thickness and morphology compared to the spheroidal type. Both nodule types contain a substantial amount of angular aluminosilicate detrital material.

Scanning Electron Microscopy (SEM) reveals prevalent microglobular and twisted fibrous structures within the nodules (Figure 5). Energy-dispersive X-ray spectroscopy (EDS) analysis indicates that the composition of these microglobular aggregates corresponds to the bulk geochemical classification of the nodules: they are Mn-rich and Fe-poor in Mn-rich nodules (sites ACB51-079, ACB51-086, Figures 5c, d, e) and Fe-rich and Mn-poor in the Fe-rich nodule (site ACB51-080, Figure 5f). Furthermore, SEM imaging identifies distinct biomorphic structures, including manganese oxide pseudomorphs after diatom frustules and microbial biofilms (Figures 5h, i).

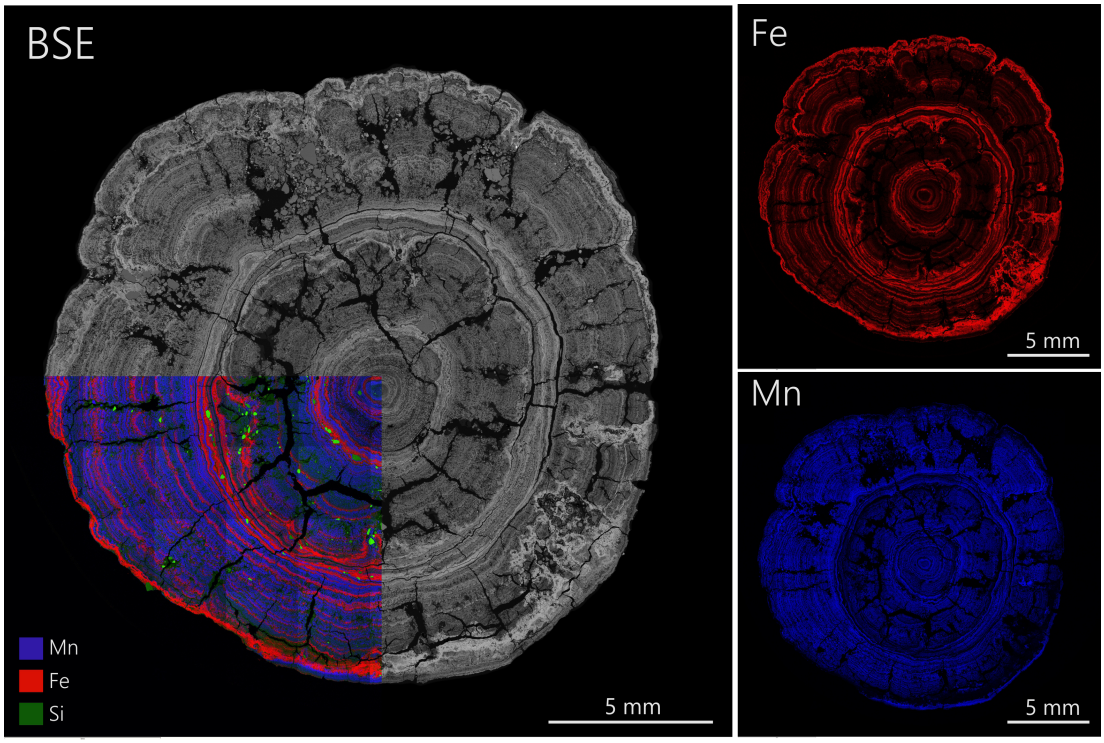

FIGURE 3
Microtextures and element distribution for Fe-rich nodule sample from site ACB51-080. Backscattered (BSE) image; Fe-Mn distribution and distribution of major element associations.

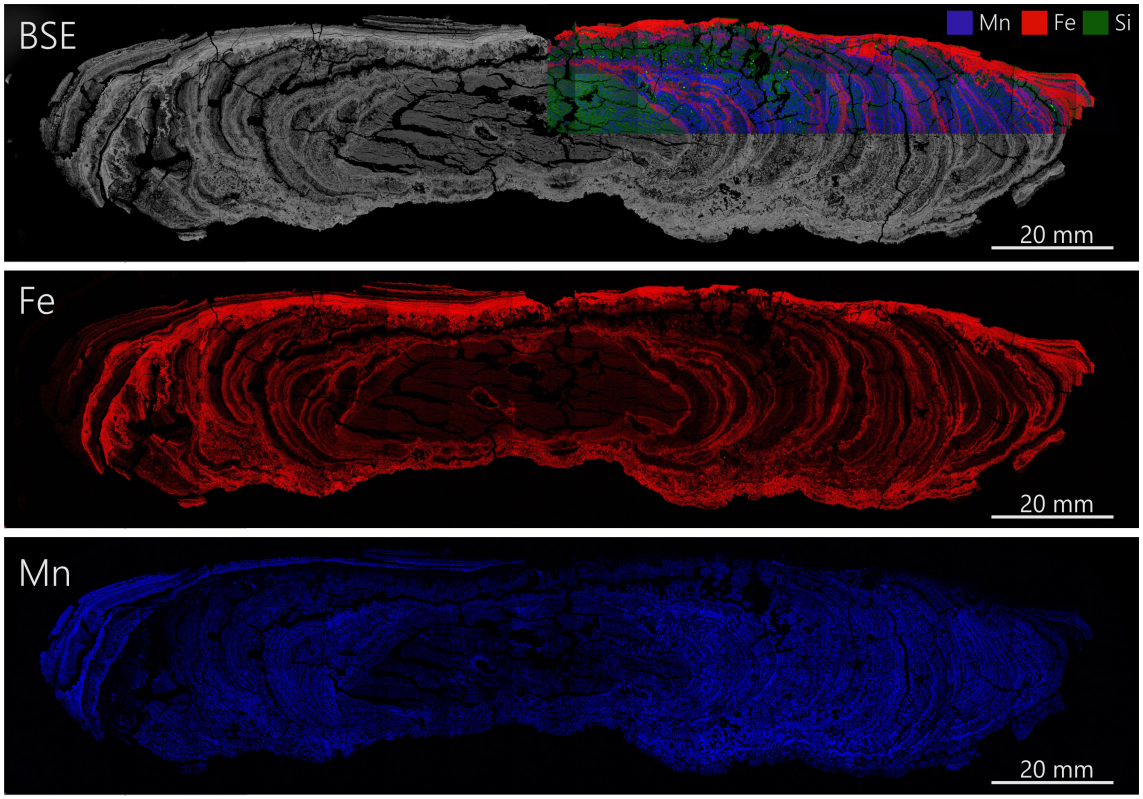

FIGURE 4
Microtextures and element distribution for Mn-rich nodule sample from site ACB51-079. Backscattered (BSE) image; Fe-Mn distribution and distribution of major element associations.

3.3 Geochemistry

3.3.1 Geochemistry of Fe-Mn nodules

The bulk concentrations of major, trace, and REY elements in the Fe-Mn nodules and their distinct parts are presented in Table 2. Based on their geochemical characteristics, the samples can be divided into two main types: Fe-rich and Mn-rich nodules.

The Fe-rich nodules (from sites ACB51–080 and ACB51-084) contain an average of 23.2% Fe and 7.04% Mn. In contrast, the Mn-rich nodules (from sites ACB51-078, ACB51-079, and ACB51-086) contain an average of 8.78% Fe and 19.1% Mn. This compositional difference is reflected in the Mn/Fe ratio, which averages 0.30 for the Fe-rich type and 2.18 for the Mn-rich type. Furthermore, Mn-rich nodules contain 3–5 times more Mn, Cd, Cu, Ni, and Mo, and 11 times more Tl than the Fe-rich nodules.

The internal geochemical heterogeneity of Mn-rich nodules was investigated by analyzing their distinct parts (Table 2). In a discoidal nodule from site ACB51-079, the composition of the top (water-facing) part was compared to that of the bottom (sediment-facing) part. Similarly, for five spheroidal nodules from site ACB51-086, a comparison was made between the outer and inner layers. In both cases, no significant differences in major, trace, or REY element concentrations were found between the contrasting nodule parts.

Compared to the upper oxidized layer of the underlying sediments, the two nodule types show distinct trace element accumulation patterns. In Mn-rich nodules, the concentrations of several elements are substantially higher than in the sediments: Mn (x42), Cd, Co, Ni (x11 each), Mo (x110), W (x8), As (x21), Tl (x7), and Fe (x4). In Fe-rich nodules, the contrast with the sediments is even more pronounced for some elements. These nodules contain 150 times more As and Mo, 41 times more Mn, 20 times more Fe, 16 times more Co, and 15 times more W. The accumulation of Ni (x7) and Cd (x3) is lower, and Tl is depleted than in the Mn-rich type.

The total concentration of rare earth elements and yttrium (ΣREY) in the studied nodules is low (186–447 ppm) compared to deep-sea diagenetic nodules from the Clarion-Clipperton Fracture Zone (CCFZ) (410–944 ppm; median: 607 ppm (Reykhard and Shulga, 2019), and shows insignificant variation across all studied samples and sampling sites (Supplementary Figure S1, Table 2). The normalized REY patterns display a clear enrichment of light REE over heavy REE, with LREE/HREE ratios ranging from 1.45 to 1.94. All samples are characterized by a negative cerium (Ce) anomaly and a positive yttrium (Y) anomaly.

3.3.2 Geochemistry and lithology of the underlying sediments

The bulk chemical composition of the underlying sediments is shown in Table 3, with corresponding grain size and lithology data provided in Supplementary Table S1, Figure 6. The Fe content in

10.3389/fmars.2025.1717972

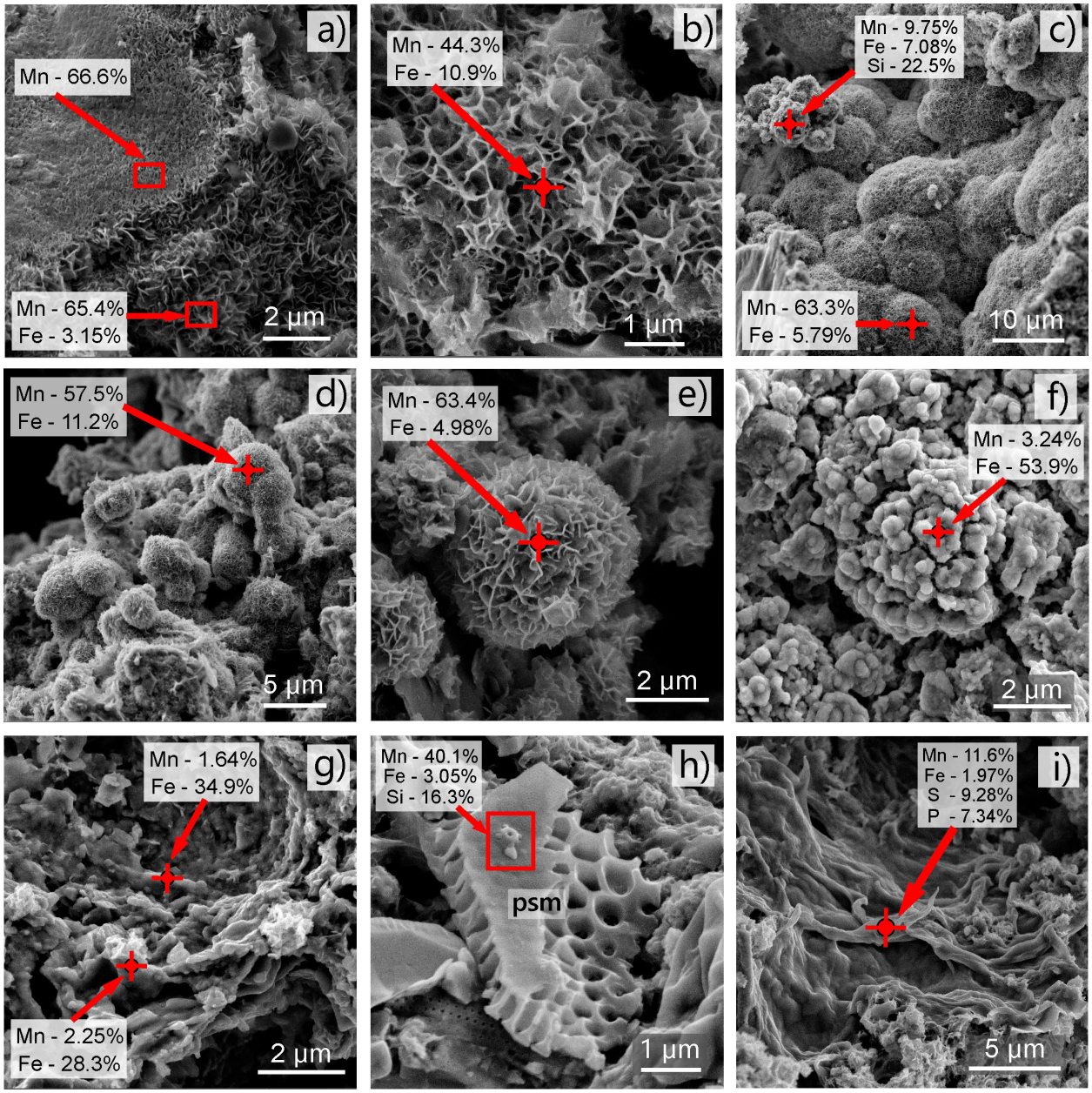

FIGURE 5
Microtextural and structural features of the Fe-Mn nodule inner parts from sites ACB51-079, ACB51-080, and ACB51-086. SEM images show: **(a, b)** Fibrous structures. **(c, d)** Mn-rich microglobular aggregates. **(e)** A twisted fibrous structure forming a globule. **(f)** Fe-rich microglobular aggregates. **(g)** Colloform textures. **(h)** psm - mineral pseudomorph after diatom frustrule. **(i)** Biofilms.

the upper oxidized layer ranges from 0.90 to 3.91%, reaching a maximum at site ACB51-086. In the underlying, reduced, fine-grained horizons, Fe content is higher, reaching up to 13%. Mn content, which is highest in the surface sediments at sites ACB51-078 (0.81%) and ACB51-086 (1.90%), decreases markedly at site ACB51-084 (0.05%), where sandy sediments prevail. A general downcore decrease in Mn concentration is observed throughout the studied sites. In the surface oxidized layer, Mn is enriched by a factor of 2–3.5 compared to the underlying reduced sediments at sites ACB51-079, ACB51-080, and ACB51-084. A markedly stronger enrichment was observed at site ACB51-078 (11-fold) and reached a maximum at site ACB51-086 (36-fold), where an increased accumulation of spheroidal Mn-rich nodules was found. The abundances of the rest of the major, trace, and rare-earth elements (REY) in the underlying sediments are generally similar across all sampling sites.

Macroscopic description, based on granulometric analysis, showed that the underlying sediments in the upper part of the studied interval are predominantly represented by bioturbated brown sand, silty sand, and sandy silt with shell fragments and rock clasts (Supplementary Table S1). Downcore, the sediments become finer-grained, more plastic, and acquire grayish and dark hues.

TABLE 2 Element composition of Fe-Mn nodules from the Gulf of Finland, Baltic Sea. $Ce_{anomaly}$ = (2 × CeSN)/(LaSN + NdSN). LREE/HREE = (LaSN + 2 × PrSN + NdSN)/(ErSN + TmSN + YbSN + LuSN).

Sample	ACB51-078	ACB51- 079						ACB51-080	ACB51-084	ACB51- 086				
	bulk (n=8)	S1	M2	M2 (top)	M2 (bottom)	M5	L2	bulk (n=11)	bulk (n=9)	Micronodules bulk (n=10)	SE bulk (n=8)	SG bulk (n=8)	SG (outer) (n=5)	SG (inner) (n=5)
Fe (wt. %)	11.4	10.5	11.9	16.5	12.5	9.8	12.5	15.0	31.4	14.9	7.80	8.87	8.16	11.8
Mn	14.0	21.6	19.4	14.5	20.0	12.7	19.3	12.0	2.04	12.9	23.8	22.9	20.9	18.2
Al	2.90	1.45	1.52	1.01	1.33	3.75	1.41	1.89	0.89	1.88	1.82	1.81	1.34	2.15
Ca	1.36	1.42	1.46	1.51	1.66	1.33	1.34	1.42	1.35	1.13	1.41	1.43	1.32	1.18
K	1.81	1.60	1.66	0.97	1.19	2.62	1.45	1.23	0.42	1.45	1.52	1.55	1.36	1.70
Na	1.24	1.10	1.08	0.93	1.02	1.33	1.01	0.96	0.52	1.02	1.00	1.00	0.88	1.05
Mg	1.18	1.27	1.16	0.91	1.29	1.48	1.01	0.88	0.66	0.83	1.33	1.24	1.06	1.10
P	1.30	1.36	1.50	2.20	1.77	0.85	1.75	2.03	3.40	1.54	0.72	0.94	0.93	1.12
S	0.14	0.18	0.16	0.15	0.16	0.12	0.18	0.12	0.06	0.14	0.22	0.21	0.20	0.17
Ti	0.17	0.08	0.07	0.05	0.07	0.22	0.07	0.10	0.05	0.10	0.10	0.10	0.08	0.12
Mn/Fe	1.24	2.05	1.63	0.88	1.60	1.29	1.54	0.80	0.07	0.87	3.04	2.59	2.57	1.55
As (ppm)	157	152	161	281	182	124	189	223	319	193	117	116	123	133
Ba	2059	3225	2866	2145	2532	2158	3411	2641	1045	3948	4377	4522	3966	4601
Be	1.28	0.94	0.95	0.86	1.65	1.67	0.98	0.95	1.63	1.56	1.77	1.40	1.25	1.70
Bi	0.26	0.20	0.22	0.19	0.19	0.22	0.22	0.17	0.16	0.17	0.25	0.19	0.19	0.15
Cd	3.21	4.95	4.09	2.32	3.74	4.25	3.03	1.77	0.68	3.52	12.9	8.17	9.57	3.28
Co	97.9	119	128	121	118	80.4	132	119	43.9	176	121	129	113	139
Cr	27.2	11.3	12.2	10.2	33.7	47.5	11.7	18.7	16.3	18.4	13.1	12.9	17.4	16.5
Cs	2.17	1.10	1.02	0.66	1.00	2.94	1.06	1.37	0.56	1.09	1.18	1.07	0.81	1.31
Cu	29.3	44.5	37.0	4.4	28.4	29.5	29.5	4.45	21.5	12.2	76.8	36.9	51.8	23.3
Ga	13.2	10.6	9.42	6.67	8.56	14.7	9.07	7.92	2.56	7.71	11.0	10.4	8.91	9.55
Hf	2.18	1.80	1.49	0.76	1.00	2.14	1.09	1.63	1.68	1.71	2.09	2.00	1.39	2.18
Li	17.6	14.6	9.34	4.13	19.5	24.3	5.90	7.35	3.08	5.79	14.0	12.8	9.90	10.9
Mo	239	495	425	284	365	293	331	113	48.8	174	686	590	479	428
Nb	8.29	5.14	4.68	3.63	4.18	9.61	5.02	5.10	5.83	5.87	6.29	5.85	4.25	6.73

(Continued)

10.3389/fmars.2025.1717972

TABLE 2 Continued

Sample	ACB51-078	ACB51- 079						ACB51-080	ACB51-084	ACB51- 086				
	bulk (n=8)	S1	M2	M2 (top)	M2 (bottom)	M5	L2	bulk (n=11)	bulk (n=9)	Micronodules bulk (n=10)	SE bulk (n=8)	SG bulk (n=8)	SG (outer) (n=5)	SG (inner) (n=5)
Ni	170	190	188	126	201	203	158	74.2	26.3	162	467	302	346	133
Pb	27.4	20.2	22.7	24.5	18.6	16.8	23.4	14.9	27.1	30.9	46.6	28.0	33.0	16.2
Rb	59.3	32.8	29.3	18.9	27.9	78.7	28.6	35.1	15.8	31.6	36.6	34.5	24.4	38.9
Sb	3.70	3.59	3.12	2.47	3.67	3.65	3.29	2.05	1.18	3.10	6.10	4.99	6.37	1.97
Sc	5.92	2.50	2.34	1.76	2.55	8.44	2.55	3.71	1.89	3.60	3.04	2.95	2.76	3.87
Sn	1.11	0.47	0.67	0.21	0.63	1.52	0.49	0.49	0.20	0.31	0.98	0.85	0.69	0.74
Sr	532	731	775	795	673	503	991	931	511	629	623	654	610	630
Ta	1.15	0.53	0.37	0.26	0.22	0.87	0.35	0.41	0.28	0.34	0.89	0.40	0.26	0.42
Th	6.69	3.24	3.15	2.13	2.65	7.97	3.36	4.09	7.46	4.14	4.60	4.29	3.15	5.04
Tl	3.92	4.85	3.57	1.79	6.09	7.19	2.33	0.91	0.11	2.58	12.0	8.46	10.1	3.76
U	10.5	14.9	13.7	12.3	11.0	11.3	14.6	12.0	13.8	15.4	15.4	15.6	13.4	18.4
V	115	104	109	101	96.2	136	106	97.2	100	112	120	103	111	119
W	13.2	11.9	10.2	7.04	6.61	6.65	15.2	10.5	6.41	6.34	7.70	6.14	8.43	5.24
Zn	244	197	177	135	237	250	170	186	207	446	615	472	583	198
Zr	77.7	64.1	60.0	32.4	40.2	73.5	42.5	56.6	72.0	69.3	81.1	72.8	53.7	83.1
La	42.6	39.6	42.9	44.7	42.8	45.0	42.2	42.6	62.8	72.3	82.9	66.3	58.8	63.1
Ce	64.5	54.6	61.3	62.3	66.8	71.0	59.3	68.7	79.5	148	175	133	122	122
Pr	9.17	7.90	9.07	9.21	9.29	9.07	8.86	8.88	13.1	14.4	18.1	13.5	11.9	13.6
Nd	36.5	34.1	37.4	39.2	36.4	36.7	37.6	36.1	51.9	60.0	73.1	56.2	48.8	56.0
Sm	6.33	6.21	6.64	7.07	6.79	6.78	6.72	6.91	9.42	10.6	13.6	10.0	8.96	10.3
Eu	0.92	0.76	0.99	1.00	0.98	0.88	0.85	1.03	1.54	1.49	1.88	1.36	1.15	1.38
Gd	6.20	5.56	6.37	6.13	6.06	5.74	5.98	6.06	8.10	9.33	11.9	8.99	7.80	8.98
Tb	0.81	0.80	0.91	0.86	0.86	0.82	0.85	0.83	1.13	1.32	1.69	1.25	1.04	1.25
Dy	4.95	4.66	5.12	4.85	4.84	4.77	4.85	4.68	6.34	7.17	9.30	6.88	6.17	6.76
Y	28.4	25.6	27.6	27.3	27.7	29.1	28.1	27.3	36.5	37.7	47.1	36.9	30.9	36.2

(Continued)

10.3389/fmars.2025.1717972

10.3389/fmars.2025.1717972

TABLE 2 Continued

Sample	ACB51-078	ACB51- 079					ACB51-080	ACB51-084	ACB51- 086			
	bulk (n=8)	S1	M2	M2 (top)	M2 (bottom)	M5	L2	bulk (n=11)	bulk (n=9)	Micronodules bulk (n=10)	SE bulk (n=8)	SG bulk (n=8)	SG (outer) (n=5)	SG (inner) (n=5)
Ho	0.96	0.89	1.00	0.94	0.94	0.90	0.96	0.91	1.22	1.33	1.75	1.26	1.13	1.29
Er	2.69	2.53	2.89	2.68	2.59	2.59	2.76	2.52	3.31	3.51	4.82	3.41	3.10	3.56
Tm	0.37	0.36	0.39	0.36	0.35	0.37	0.39	0.36	0.43	0.48	0.68	0.49	0.40	0.49
Yb	2.48	2.34	2.47	2.33	2.33	2.34	2.47	2.37	2.81	3.04	4.30	3.34	2.63	3.10
Lu	0.35	0.34	0.37	0.34	0.32	0.37	0.36	0.32	0.38	0.45	0.63	0.50	0.59	0.45
ΣREY	207	186	205	209	209	216	202	210	272	371	447	343	305	329
Ce an	0.71	0.67	0.67	0.67	0.73	0.76	0.67	0.77	0.62	0.99	0.98	0.96	1.00	0.91
Y an	1.18	1.16	1.11	1.16	1.18	1.29	1.17	1.20	1.25	1.14	1.08	1.17	1.09	1.12
LREE/ HREE	1.55	1.45	1.50	1.66	1.66	1.58	1.51	1.62	1.94	1.98	1.72	1.75	1.66	1.79

SN shale normalized.

3.4 Organic geochemical parameters of Fe-Mn nodules and underlying sediments

The composition of n-alkanes and organic geochemical parameters in the studied samples are presented in Table 4. The total organic carbon (TOC) content in the nodules ranges from 1.0 to 2.6%. The concentrations of total lipid extract (TLE) in the nodules ranged from 54.3 to 115 μg/g dry weight (average of 75.9 μg/g dw). The n-alkane concentrations varied from 0.50 to 2.50 μg/g dry weight, which is comparable to their content in the underlying sediments. n-Alkanes from C_{14} to C_{33}, as well as the isoprenoids pristane and phytane, were detected in all samples. The n-alkane distributions in the nodules are predominantly bimodal. The low molecular weight (LMW) homologs show a C_{max} at C_{16} and C_{18}, while the high molecular weight (HMW) compounds have a C_{max} at C_{27}, C_{29}, and C_{31} (Figures 7a-h). Sample ACB51-079(L2) is an exception, exhibiting a unimodal distribution with a pronounced abundance of middle molecular weight components (Figure 7d). The carbon preference index (CPI) values are high for the HMW fractions (average CPI = 3.1) and low for the LMW fractions (average $OEP_{17\text{-}19}$ = 0.67). The $\Sigma C_{12}–C_{14}/\Sigma C_{25}–C_{33}$ ratio varies significantly between sampling sites, from 0.68 to 2.60. The highest value was observed in the large, discoidal nodule sample ACB51-079(L1). Pristane (Pr) and phytane (Ph) were present in all samples, with a ratio Pr/Ph < 1, except for sample ACB51-079(S1), which had a Pr/Ph ratio of 1.26.

In the underlying sediments, the TOC content is generally lower (0.70 to 0.89%) than in the nodules, with the exception of site ACB51-086, which showed a significantly higher value of 3.28%. In contrast, the TLE content in the sediments is substantially higher (by a factor of 5 to 15) than in the nodules, despite comparable n-alkanes concentrations. The sediments are characterized by a bimodal n-alkane distribution with a strong prevalence of HMW components compared to the nodules. This is reflected in the lower $\Sigma C_{12}–C_{24}/\Sigma C_{25}–C_{33}$ ratio, which ranges from 0.45 to 0.60 (Figures 7 i-l, Table 4). The $OEP_{17–19}$ values in the underlying sediments are similar to those determined in the Fe-Mn nodules, whereas CPI values are higher (5.04 on average).

3.5 Regularized canonical correlation analysis

This study investigates the multivariate relationship between elemental composition and organic biomarker signatures in Fe-Mn nodules from two contrasting ore formation environments: the shallow-water Baltic Sea and the deep-ocean Clarion-Clipperton Fracture Zone (CCFZ) in the Pacific Ocean. To ensure a consistent comparative analysis, an identical suite of major/trace elements and n-alkane biomarkers was measured for all samples using same analytical procedures. The dataset for the Baltic Sea nodules was obtained in this study, while for the CCFZ nodules data from (Shulga, 2017, Shulga, 2018) were used.

The rCCA results are visualized in a correlation biplot (Figure 8a) and a sample score plot (Figure 8b), which are interpreted conjointly. In the biplot, the cosine of the angle between variable vectors

TABLE 3 Element composition of underlying sediments from the Gulf of Finland, Baltic Sea. $Ce_{anomaly}$ = (2 × CeSN)/(LaSN + NdSN). LREE/HREE = (LaSN + 2 × PrSN + NdSN)/(ErSN + TmSN + YbSN + LuSN).*SN* shale normalised.

Sample	ACB51- 078		ACB51- 079			ACB51- 080		ACB51- 084			ACB51- 086		
Interval, cm	0-0.5	0.5-2	0-1	1-8	8-10	0-2	2-4	0-0.5	0.5-1.5	1.5-4	0-2	4-6	6-6.5
Fe (wt. %)	1.84	4.73	2.29	5.69	13.6	0.90	6.42	1.29	1.03	4.37	3.91	3.33	5.98
Mn	0.81	0.07	0.29	0.08	0.63	0.31	0.09	0.05	0.02	0.05	1.90	0.05	0.07
Al	5.68	9.02	6.04	9.26	8.22	3.99	10.0	5.87	5.44	8.25	5.60	6.81	9.37
Ca	0.99	1.28	0.98	1.26	1.29	0.70	0.93	0.93	0.82	1.05	1.04	1.10	0.79
K	2.62	3.38	2.56	3.70	2.92	1.87	3.39	3.00	2.78	3.31	2.27	2.82	3.75
Na	1.92	1.95	1.90	2.07	1.65	1.35	1.47	1.93	1.77	1.55	1.71	1.74	1.33
Mg	0.40	1.58	0.62	1.88	1.80	0.21	2.13	0.25	0.18	1.30	0.70	0.77	1.85
P	0.11	0.08	0.09	0.08	0.68	0.08	0.09	0.06	0.03	0.07	0.25	0.08	0.08
S	0.06	0.03	0.23	0.05	0.03	0.09	0.05	0.04	0.03	0.04	0.10	0.22	0.04
Ti	0.16	0.48	0.17	0.48	0.42	0.08	0.57	0.15	0.14	0.47	0.21	0.28	0.53
Mn/Fe	0.44	0.02	0.12	0.01	0.05	0.34	0.01	0.04	0.02	0.01	0.49	0.02	0.01
As (ppm)	8.19	3.06	5.28	4.42	7.71	2.90	2.70	1.46	–	3.24	23.2	6.88	3.20
Ba	913	672	1785	689	873	1237	576	669	636	596	908	613	566
Be	2.34	3.10	2.34	3.23	2.84	1.61	3.50	2.39	2.20	2.23	2.32	2.41	2.82
Bi	0.11	0.26	0.18	0.31	0.31	0.08	0.47	0.09	0.07	0.34	0.26	0.16	0.47
Cd	0.31	0.10	0.48	0.15	0.11	0.63	0.35	0.24	0.20	0.16	0.80	0.15	0.09
Co	6.44	17.5	8.71	19.5	24.1	5.43	22.4	3.96	4.63	14.9	25.8	69.7	24.8
Cr	19.1	72.2	26.8	94.2	81.2	8.39	106	12.5	9.80	69.9	38.6	40.3	91.2
Cs	2.24	5.39	2.97	6.15	6.18	1.54	9.40	1.89	1.80	5.72	2.66	3.33	7.76
Cu	9.07	35.4	14.0	44.1	20.5	6.21	41.4	5.68	4.55	33.4	24.5	15.3	34.8
Ga	12.4	21.5	12.9	23.9	20.4	7.98	24.2	12.4	12.2	21.2	13.3	14.6	26.0
Hf	4.29	5.01	2.69	4.55	3.29	3.09	4.04	6.30	8.69	5.26	5.27	7.97	4.58
Li	14.0	43.5	17.4	50.0	44.5	8.91	58.7	12.9	11.3	41.6	16.1	22.9	57.4
Mo	4.18	1.03	2.38	1.37	8.64	0.68	1.07	0.34	0.45	2.56	19.9	13.2	2.34
Nb	9.49	21.7	7.96	21.8	18.9	4.56	20.5	14.3	9.52	19.6	10.3	13.4	21.3
Ni	10.9	44.6	18.3	53.7	46.2	7.24	55.3	6.03	4.83	37.2	37.0	48.9	55.4
Pb	19.9	23.1	23.3	24.0	19.9	16.8	26.8	22.7	20.5	24.6	37.0	20.4	28.9
Rb	120	169	146	178	165	103	219	126	130	167	118	127	201
Sb	0.68	0.26	0.82	0.30	0.66	0.41	0.43	0.22	0.17	0.43	1.43	0.43	0.48
Sc	5.27	17.3	6.80	19.9	17.4	2.65	23.3	4.18	4.02	16.4	8.21	10.1	19.1
Sn	1.11	1.91	0.98	2.89	2.65	0.89	2.80	0.91	0.62	2.90	1.65	1.01	3.15
Sr	193	194	207	187	278	145	147	154	144	180	218	166	145
Ta	0.53	1.28	0.59	1.27	1.04	0.33	1.56	0.82	0.52	1.17	0.95	0.77	1.41
Th	6.56	16.0	8.73	17.0	15.4	3.79	20.3	4.72	6.41	18.7	8.33	12.3	19.3
Tl	0.69	0.86	0.86	1.01	0.87	0.62	1.21	0.72	0.62	1.18	0.86	0.80	1.31
U	2.29	4.10	2.43	4.21	4.31	1.48	7.48	1.64	1.97	5.11	3.98	6.63	12.4

(Continued)

TABLE 3 Continued

Sample	ACB51- 078		ACB51- 079			ACB51- 080		ACB51- 084			ACB51- 086		
Interval, cm	0-0.5	0.5-2	0-1	1-8	8-10	0-2	2-4	0-0.5	0.5-1.5	1.5-4	0-2	4-6	6-6.5
V	31.7	109	37.3	129	122	7.49	150	18.7	16.5	101	51.5	62.3	140
W	1.91	1.51	1.02	1.49	3.64	0.49	1.88	0.69	0.48	1.54	2.19	0.86	1.76
Zn	50.6	106	75.8	135	162	49.3	149	39.4	30.4	108	144	68.0	134
Zr	177	190	91.3	177	127	118	150	314	364	198	217	335	160
La	29.6	58.9	25.3	56.5	53.6	20.0	63.3	25.4	26.7	50.5	38.2	46.2	57.2
Ce	54.2	113	52.3	108	101	38.1	130	46.2	46.8	108	83.0	86.2	128
Pr	6.42	13.4	5.68	12.91	11.9	4.30	15.4	5.52	5.58	12.0	9.66	10.5	14.1
Nd	24.2	49.7	21.6	47.8	44.4	15.9	53.3	21.7	21.5	44.7	34.4	40.9	50.7
Sm	4.69	9.60	4.14	8.97	8.40	3.00	9.89	4.24	4.14	8.41	6.56	8.03	9.66
Eu	0.94	1.54	0.94	1.40	1.21	0.72	1.57	1.10	1.05	1.42	1.16	1.35	1.61
Gd	3.62	7.22	3.48	6.67	6.38	2.43	7.77	3.37	3.17	7.32	5.34	6.24	7.72
Tb	0.55	1.09	0.51	1.03	0.96	0.38	1.15	0.55	0.50	1.14	0.81	0.95	1.05
Dy	3.28	6.23	2.93	6.01	5.50	2.08	6.09	3.43	3.19	6.06	4.51	5.67	6.51
Y	18.2	35.9	17.7	33.6	32.7	12.4	32.7	17.4	18.0	30.1	26.9	33.6	28.0
Ho	0.62	1.20	0.59	1.14	1.03	0.41	1.20	0.66	0.60	1.19	0.90	1.09	1.22
Er	1.75	3.39	1.74	3.19	2.93	1.23	3.35	1.98	1.82	3.36	2.59	3.21	3.61
Tm	0.25	0.49	0.25	0.45	0.41	0.17	0.47	0.29	0.27	0.49	0.37	0.44	0.50
Yb	1.91	3.67	1.97	3.40	3.07	1.29	3.49	2.20	2.11	3.24	2.74	3.38	3.42
Lu	0.25	0.48	0.25	0.45	0.41	0.17	0.48	0.31	0.29	0.50	0.36	0.46	0.44

SN shale normalised.

approximates their correlation, and vector length reflects the variable contribution to the canonical components. The score plot displays samples in the space of these components, where proximity indicates multivariate similarity. The correlation biplot demonstrates a pronounced segregation of variables along CV1. The positive end of CV1 is dominated by elements including Co, Ni, W, Mo, Mn, S, and Ba. In contrast, the negative end is characterized by terrigenous, marine, and bacterially-derived biomarkers, along with organic matter parameters (TLE, TOC, $OEP_{17\text{-}19}$), and elements such as P, As, and Fe, indicating a strong negative correlation between these two multivariate patterns. This divergence in variable space is directly mirrored by the sample distribution. The score plot shows a clear separation of samples into two distinct clusters based on their geographic origin. All CCFZ samples plot with positive scores on CV1, while all Baltic Sea samples have negative scores.

4 Discussion

4.1 Regional context and genesis of Baltic Sea nodules

The geochemical data reveal a clear division into Fe-rich and Mn-rich nodule types across the study sites, yet no systematic correlation is observed between nodule morphology, geographic location, and the properties of the underlying sediments. This indicates that the formation of distinct geochemical types is governed by localized microenvironments rather than broad-scale sedimentary patterns.

The elemental composition of the studied nodules aligns with previously reported data from other parts of the Baltic Sea (Zhamoida et al., 1996, Zhamoida et al., 2007; Glasby et al., 1997; Zhang et al., 2002; Baturin, 2009), confirming regional geochemical consistency. Comparison with data for Arctic Fe-Mn nodules from the Kara (Baturin, 2011; Menendez et al., 2018; Vereshchagin et al., 2019; Shulga et al., 2022), East Siberian (Baturin and Dubinchuk, 2011; Sattarova et al., 2025), Chukchi (Baturin and Dubinchuk, 2011; Kolesnik and Kolesnik, 2013; Cui et al., 2020) and Barents (Ingri and Pontér, 1987) seas also indicates their similar elemental composition (Supplementary Table S5). In general these shallow-water fast-growing deposits exhibit lower Mn content compared to deep-sea nodules from the Clarion-Clipperton Zone and Peru Basin, while maintaining higher Fe concentrations (Hein and Koschinsky, 2014). All studied samples display low Cu+Ni+Co content (<1.5%) and highly variable Mn/Fe ratios (0.07-3.04), which complicates their classification using conventional genetic diagrams. Application of the Bonatti ternary diagram (Fe-Mn-

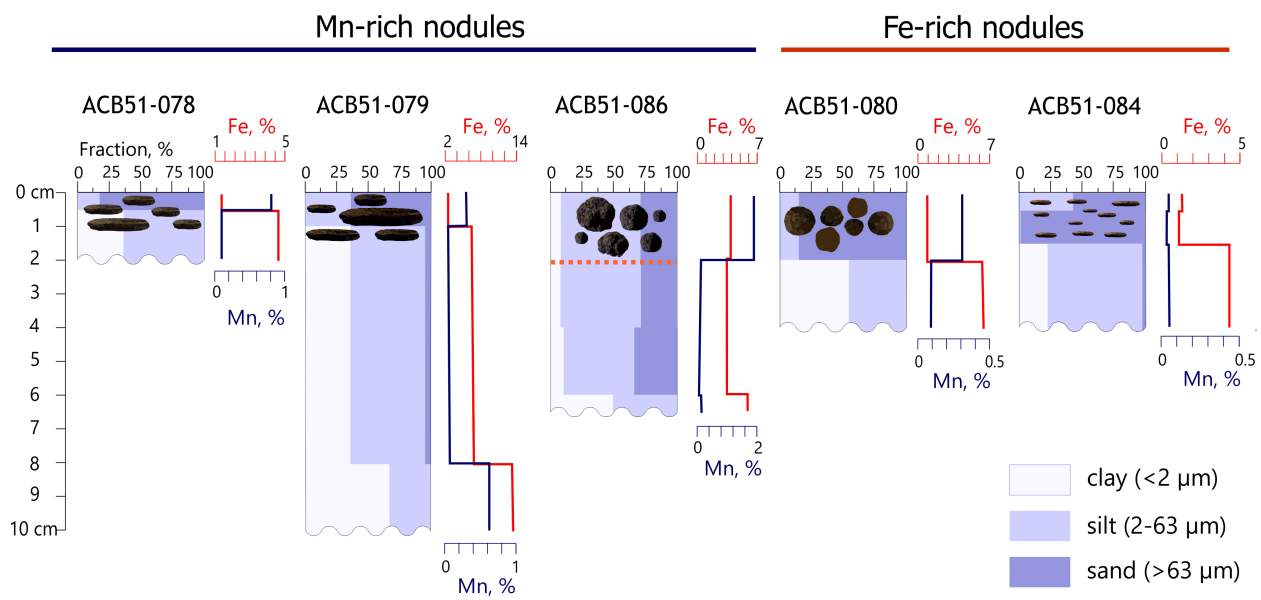

FIGURE 6
Grain-size distribution, major elements (Fe, Mn) content in the underlying sediments, and morphology of Fe-Mn nodules across the sampling sites. The orange dot line shows cemented Fe-Mn nodules of various sizes forming a discontinuous crust (see description in Supplementary Table S1). Step plot showing the downcore distribution of Fe and Mn concentrations (%) in the underlying sediments.

(Cu+Ni+Co)×10) (Bonatti et al., 1972) yields uncertain results for these deposits, highlighting the limitation of classification schemes developed for slow-growing deep-ocean ore deposits when applied to fast-growing diagenetic types (Menendez et al., 2018). According to Bau (Bau et al., 2014) the rare earth element and yttrium (REY) patterns provide more reliable genetic indicators (Figure 9). The consistent negative Ce anomaly, Y/Ho ratio close to 1, and intermediate Nd concentrations (~46 ppm) collectively point to a dominant diagenetic origin, consistent with previous studies of Baltic Sea (Baturin, 2009) and Kara Sea (Baturin, 2011; Vereshchagin et al., 2019; Shulga et al., 2022) Fe-Mn deposits. The general depletion of many major and trace elements, including REY, can be attributed to the high growth rates of these nodules, which results in dilution of authigenic components by detrital material during rapid accretion.

The Fe-Mn layer intercalations observed in thin sections reflects their differential redox behavior, recording rapid fluctuations in depositional conditions. In the dynamic Baltic Sea environment, redox oscillations occur periodically across the study region (Glasby et al., 1997). During temporary oxygen depletion in sediments, Mn and Fe are remobilized and diffuse upward. Mn-rich layers typically form during relatively stable bottom conditions when the reduced sediments are covered by an intact oxidized surface layer. Conversely, erosion of this oxic layer by bottom currents can facilitate Mn loss to the water column (with its further carrying out by bottom currents) while promoting the formation of Fe-rich phases (Bogdanov et al., 1995; Rozanov, 2015). Site-specific variations in sediment composition and redox layer thickness further modulate these processes. Despite the close proximity of the study sites, the underlying sediments exhibit variations in the proportions of granulometric fractions and in the thickness of the upper oxidized layer hosting the nodules (Figure 6, Supplementary Table S1). The maximum thickness of the oxidized sediment layer observed at site ACB51-086, which contains abundant spheroidal Mn-rich nodules, exemplifies how local conditions can create particularly favorable environments for nodule formation and preservation. The presence of micronodules along with the microglobular surfaces of the spheroidal samples at site ACB51–086 indicates that growth is ongoing. This interpretation is supported by the co-occurrence of nodules of all sizes within the same sedimentary interval (Figure 1), together with a geochemical trend marked by increasing Mn/Fe ratios with nodule size (Table 2), suggesting contemporary formation rather than multiple burial events.

The prevalence of microglobular structures across all samples, as revealed by SEM, implies a common formation *via* precipitation from supersaturated solutions (Figure 5). The chemical composition of these globules mirrors the bulk nodule composition (Mn-rich in Mn-dominated types, Fe-rich in Fe-rich types), indicating that the same fundamental process yields different mineral phases depending on the local chemical environment. The presence of manganese oxide pseudomorphs after diatom frustules, along with extensive microbial biofilms, points to active biogeochemical interactions and biologically mediated mineralization processes within the nodules. Similar biomineral structures have been documented in both Arctic (Shulga et al., 2022) and deep-sea (Wang et al., 2012; Wu et al., 2013; Reykhard and Shulga, 2019; Jiang et al., 2020) ferromanganese nodules, suggesting widespread occurrence of these microbially influenced formation mechanisms.

TABLE 4 The concentration of total organic carbon (%), grouped n-alkanes (ng/g dry weight and %) and organic-geochemical index in Fe-Mn nodules and underlying sediments from the Gulf of Finland, Baltic Sea.

Site	ACB51- 078 bulk (N=8)	ACB51- 079				ACB51- 080 bulk (N=11)	ACB51- 084 bulk (N=9)	ACB51- 086		ACB51- 079 (0-1 cm)	ACB51- 080 (0-2 cm)	ACB51- 084 (0-0,5 cm)	ACB51- 086 (0-2 cm)
		S1	M2	M5	L2			SE (N=8)	SG (N=8)				
	Fe-Mn nodules									Sediments			
TOC, %	1.68	1.46	1.02	1.60	1.41	2.02	2.57	1.97	1.63	0.89	0.70	0.75	3.28
Pr/Ph	0.43	1.26	0.55	0.68	0.56	0.35	0.18	0.48	0.58	0.64	0.68	1.01	0.86
OEP_{17-19}	0.73	0.65	0.62	0.54	0.64	0.71	0.77	0.76	0.64	0.83	0.85	0.71	0.92
CPI	3.25	3.03	2.95	3.78	2.42	3.44	2.94	2.91	3.46	5.12	4.75	5.75	4.54
$C_{15+17+19}$, ng/g	221	49.9	67.2	102	106	137	145	266	129	139	106	123	265
$C_{27+29+31}$, ng/g	684	133	287	625	295	367	259	443	324	895	653	675	1714
$C_{15+17+19}$, %	8.84	9.97	7.23	5.47	4.85	9.74	12.1	14.2	8.40	6.44	6.87	7.19	6.54
$C_{27+29+31}$, %	27.3	26.6	30.9	33.5	13.5	26.2	21.6	23.7	21.2	41.4	42.3	39.4	42.2
$C_{15+17+19}$/ $C_{27+29+31}$	0.32	0.37	0.23	0.16	0.36	0.37	0.56	0.60	0.40	0.16	0.16	0.18	0.15
TAR	3.09	2.67	4.28	6.13	2.78	2.69	1.78	1.67	2.52	6.44	6.15	5.48	6.46
ΣC_{14-20}, ng/g	593	134	191	324	378	401	373	668	417	414	281	401	661
$\Sigma C_{16,18,20-24}$, ng/g	981	177	308	571	1452	549	541	721	783	534	366	450	952
ΣC_{12-24}, ng/g	1253	243	381	754	1578	737	710	1029	939	734	482	643	1264
ΣC_{25-35}, ng/g	1239	254	540	1104	607	657	485	834	589	1426	1063	1068	2794
$\Sigma C_{12-24}/\Sigma C_{25-35}$	1.01	0.96	0.71	0.68	2.60	1.12	1.46	1.23	1.60	0.51	0.45	0.60	0.45
n-alkanes, μg/g	2.50	0.50	0.93	1.86	2.19	1.40	1.20	1.87	1.53	2.16	1.54	1.71	4.06
TLE, μg/g	85.1	72.0	66.5	54.3	70.1	70.7	58.3	115	90.5	409	385	829	1522

Pr – pristine, Ph – phytane, OEP_{17-19} - Odd-Even preference, CPI -Carbon preferance index, TLE - total lipid extract, $C_{15+17+19}$ – marker of marine OM, $C_{27+29+31}$ – marker of terrigenous OM, $C_{16+18+C20-24}$ – marker of bacterial-derived OM.
$OEP_{17} = (C_{15} +4\times C_{17} + C_{19})/(4\times C_{16} + 4\times C_{18})$, $OEP_{19} = (C_{17} +4\times C_{19} + C_{21})/(4\times C_{18} + 4\times C_{20})$, $OEP_{17-19} = 0.5\times(OEP_{17} + OEP_{19})$.
$CPI = 0.5\times[(C_{25} + C_{27} + C_{29} + C_{31} + C_{33}) /(C_{24} + C_{26} + C_{28} + C_{30} + C_{32}) + (C_{25} + C_{27} + C_{29} + C_{31} + C_{33}) /(C_{26} + C_{28} + C_{30} + C_{32} + C_{34})]$.

10.3389/fmars.2025.1717972

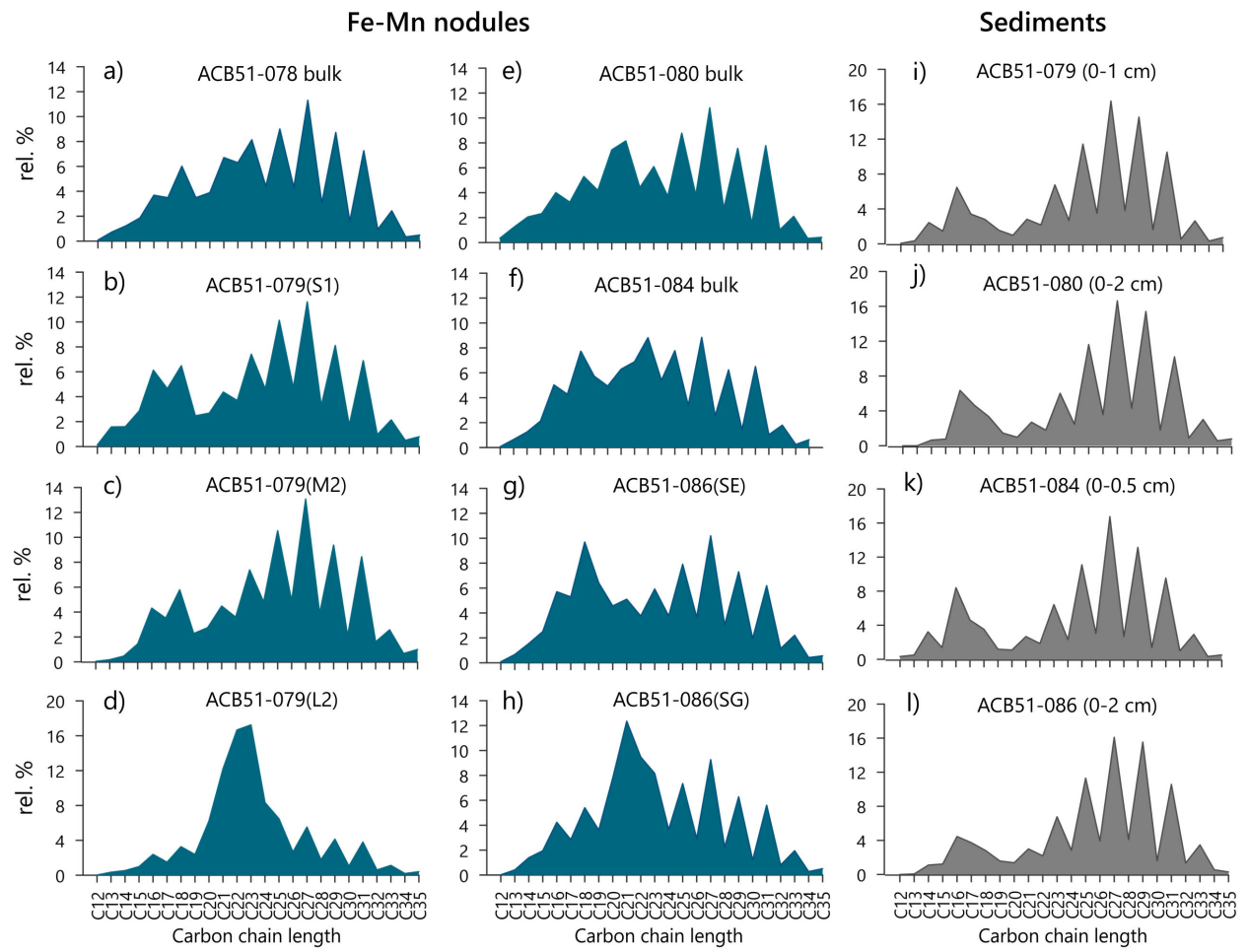

FIGURE 7
Distribution of n-alkanes in the lipid fraction of organic matter in samples of Fe-Mn nodules **(a-h)** and underlying sediments **(i-l)** from Gulf of Finland, Baltic Sea.

4.2 Organic matter sources and preservation in Fe-Mn nodules

The molecular distribution of n-alkanes is used as a proxy for determining organic matter (OM) sources and diagenetic transformations in marine sedimentary environments, including Fe-Mn deposits (Eglinton and Repeta, 2004; Killops and Killops, 2004). The n-alkane patterns in the Gulf of Finland nodules indicate a mixed OM origin, with no clear predominance of either marine or terrigenous components (Figure 7). A strong odd-over-even carbon predominance in high-molecular-weight (HMW) n-alkanes (average CPI = 3.1), with a C_{max} at C_{27}, C_{29}, and C_{31}, is characteristic of leaf waxes from higher plants that have undergone limited diagenetic alteration (Killops and Killops, 2004). The higher CPI values in the underlying sediments (average 5.04) suggest preferential incorporation of partially degraded terrigenous OM into the nodules. The exceptional preservation of this terrigenous signal is likely mediated by encapsulation within the Fe-Mn oxyhydroxide matrix, which inhibits further biodegradation. In contrast, the low molecular weight (LMW) n-alkanes and low OEP_{17-19} values (~0.67) indicate contributions from phytoplankton and microbial sources. The significant abundance of mid-chain n-alkanes (31–66% of total) provides evidence for bacterial OM production. A progressive increase in bacterial alkane concentrations is observed at site ACB51-079, rising from 177 ng/g (S size nodule) to 571 ng/g (M size) and 1472 ng/g (L size), demonstrating continuous microbial biomass accumulation throughout nodule growth. This finding aligns with 16S rRNA sequencing data from Gulf of Finland nodules (Yli-Hemminki et al., 2014), which demonstrated that microbial communities on the surface and in the porous interior of the nodules form two distinct clusters based on genetic differences. This confirms that the nodules function as active microbial habitats rather than passive OM repositories. The Pr/Ph ratio below unity in most samples suggests deposition under suboxic to anoxic conditions, consistent with the dynamic redox stratification of Baltic Sea sediments. Despite comparable n-alkane concentrations, the total lipid extract (TLE) content is substantially

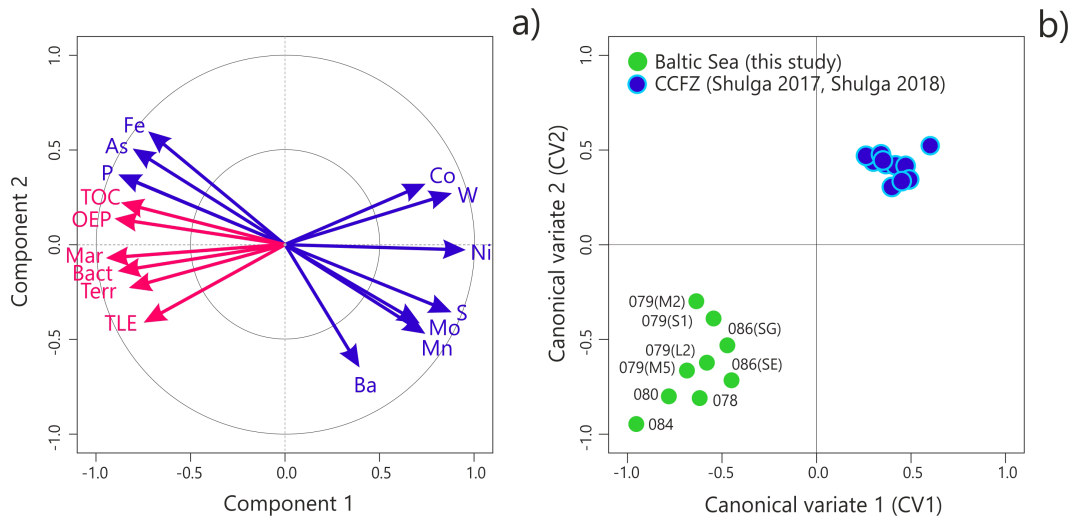

FIGURE 8
Visualization of rCCA results as a correlation biplot **(a)** and a sample score plot **(b)**. The explanation is provided in the text. TOC – content of total organic carbon, TLE – content of total lipid extract. OEP – odd to even preference index. Mar - marker of marine OM (n-alkanes $C_{15+17+19}$), Bact – marker of bacterial-derived OM (n-alkanes C_{16+18}+C_{20-24}), Terr - marker of terrigenous OM (n-alkanes $C_{27+29+31}$).

higher (by a factor of 5–15) in the underlying sediments relative to the nodules. This indicates that nodules act as selective geochemical traps, effectively preserving specific OM signatures, particularly refractory terrigenous biomarkers and products of *in-situ* microbial activity, within their mineral matrices, despite lower overall lipid content.

4.3 Integrated geochemical-biomarker relationships revealed by rCCA

The clear separation of Fe-Mn nodules along the first canonical component, as revealed by rCCA, reflects fundamentally different diagenetic regimes and timescales of formation in the Baltic Sea

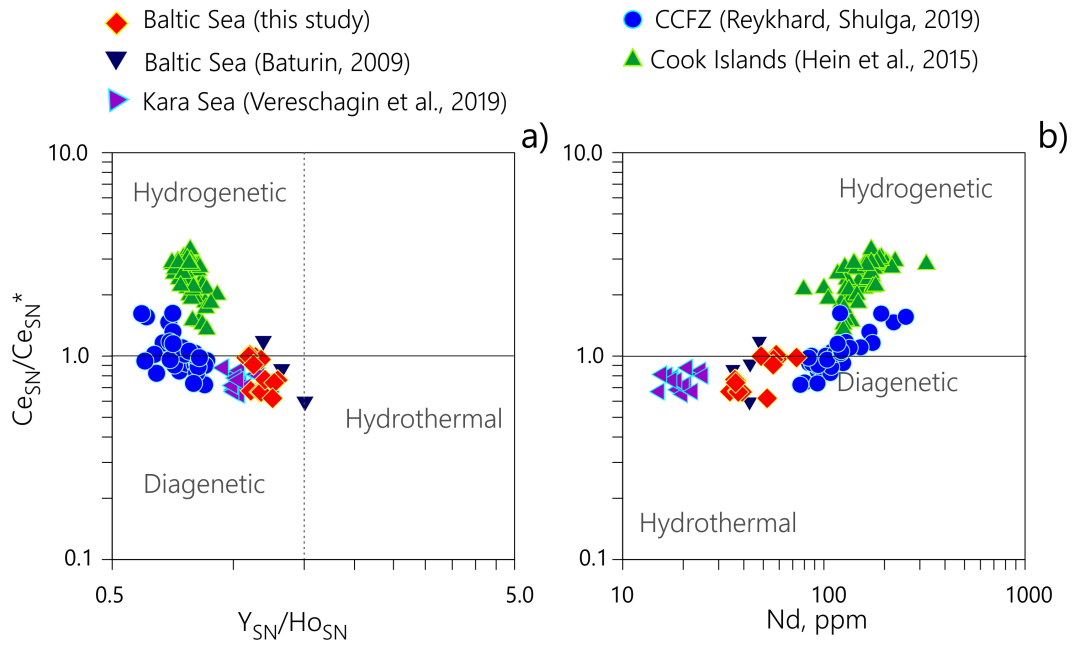

FIGURE 9
Relationship between **(a)** CeSN/CeSN* ratio vs. Nd concentration and **(b)** CeSN/CeSN* ratio vs. YSN/HoSN ratio in Fe-Mn nodule samples, where CeSN* = 0.5 × LaSN + 0.5 × PrSN and SN = shale normalized. Genetic classification follows Bau et al. (2014), with fields indicating diagenetic, hydrogenetic, and hydrothermal origins.

versus the CCFZ (Figure 8). The CCFZ cluster is associated with a classic element set for deep-sea ore deposits (Co, Ni, W, Mo, Mn). Their strong co-enrichment indicates slow, steady growth over millions of years under relatively stable abyssal conditions. While diagenetic processes certainly contribute to nodule formation in the CCFZ, they operate on immensely long, geologically stable timescales, allowing for the efficient sequestration of metals from pore waters over million years. This results in the characteristic "diagenetic-metalliferous" signature dominated by Mn, Ni, and other cations.

Conversely, the Baltic Sea cluster is defined by a set of geochemical parameters that reflect rapid nodule growth in a dynamic, redox-stratified environment. The strong association of organic matter parameters (TOC, TLE, OEP_{17-19}), biomarkers from terrigenous, marine, and bacterial sources, and redox-sensitive elements such as As and P indicates a formation process dominated by high-intensity, cyclic diagenesis. In this shallow basin, high primary productivity delivers substantial organic matter to the sediments. Its subsequent microbial degradation drives the reductive remobilization of Mn and Fe, while frequent fluctuations in redox conditions at the sediment-water interface promote the re-oxidation and precipitation of fresh Fe-Mn oxyhydroxides. These newly formed phases efficiently sequester elements like As and P, which have a high affinity for Fe-oxyhydroxides. This interpretation is directly supported by the significant scatter of the Baltic Sea samples across the lower-left quadrant of the sample score plot (Figure 9b), which reflects the high variability of these local diagenetic microenvironments. Therefore, the rCCA effectively separates two end-member diagenetic processes, distinguishing "long-term, stable diagenetic-metalliferous" type (CCFZ) from "dynamic, organic-influenced" type (Baltic Sea). This divergence underscores how regional depositional conditions and timescales of formation fundamentally govern the integrated geochemical and biomarker signature of Fe-Mn nodules.

5 Conclusions

This integrated study demonstrates that the Fe-Mn nodules from the Gulf of Finland, Baltic Sea represent a distinct shallow-water diagenetic end-member, fundamentally different from their deep-sea counterparts. Their formation occurs through the rapid remobilization and precipitation of Fe-Mn oxyhydroxides at the sediment-water interface, a process driven by the frequent redox oscillations characteristic of the shallow, productive Baltic Sea. This genesis is reflected in their geochemical signature, which is characterized by high Mn and Fe content, low Cu+Ni+Co concentrations, highly variable Mn/Fe ratio, REY depletion, and a consistent negative Ce anomaly, aligning with other fast-growing shallow-water ore deposits in the Baltic and Arctic Seas. Microtextural analysis reveals complex formation mechanisms involving both abiotic and biological processes. The prevalence of microglobular structures indicates precipitation from supersaturated solutions, while manganese oxide pseudomorphs after diatom frustules and extensive microbial biofilms provide direct evidence of biologically influenced mineralization. The nodules function as active microbial habitats, preserving refractory terrigenous organic matter within their mineral matrices while accumulating bacterially derived organic matter throughout their growth, as evidenced by the increasing concentration of bacterial-derived components with nodule size. The lack of correlation between nodule morphology, geochemical composition, and sediment properties underscores that highly localized microenvironments, rather than broad-scale sedimentary patterns, ultimately dictate nodule formation and composition. This concept is further supported by the application of regularized canonical correlation analysis (rCCA), which was used for unravel the complex relationships between elemental composition and n-alkane biomarkers. The analysis revealed a clear separation between Baltic Sea and deep-sea nodules, suggesting that differences in the quantity, quality, and degradation of organic matter may govern diagenetic processes, ultimately resulting in distinct geochemical signatures of Fe-Mn nodules across different marine environments.

Data availability statement

The original contributions presented in the study are included in the article/Supplementary Material, further inquiries can be directed to the corresponding author.

Author contributions

NS: Conceptualization, Data curation, Formal analysis, Funding acquisition, Investigation, Methodology, Visualization, Writing – original draft, Writing – review & editing. PP: Formal analysis, Methodology, Visualization, Writing – original draft, Writing – review & editing. KR: Investigation, Methodology, Visualization, Writing – original draft.

Funding

The author(s) declare financial support was received for the research and/or publication of this article. This research was funded by the Russian Science Foundation, grant number 24-27-00409.

Acknowledgments

The authors is grateful to scientific parties, masters, and crews of the R/V Akademik Sergey Vavilov (cruise 51) for their professional support in the material collection for this study. The authors gratefully acknowledge Dmitrii Borisov (Shirshov Institute of Oceanology) for his valuable suggestions that improved this manuscript, and Elena Streltsova (Shirshov Institute of Oceanology) for sample preparation.

Conflict of interest

The authors declare that the research was conducted in the absence of any commercial or financial relationships that could be construed as a potential conflict of interest.

Generative AI statement

The author(s) declare that no Generative AI was used in the creation of this manuscript.

Any alternative text (alt text) provided alongside figures in this article has been generated by Frontiers with the support of artificial intelligence and reasonable efforts have been made to ensure accuracy, including review by the authors wherever possible. If you identify any issues, please contact us.

Publisher's note

Supplementary material

The Supplementary Material for this article can be found online at: https://www.frontiersin.org/articles/10.3389/fmars.2025.1717972/full#supplementary-material

References

Bartlett, M. S. (1941). The statistical significance of canonical correlations. *Biometrika* 32, 29. doi: 10.2307/2332247

Baturin, G. N. (2009). Geochemistry of ferromanganese nodules in the Gulf of Finland, Baltic Sea. *Lithol. Miner. Resour.* 44, 411–426. doi: 10.1134/S0024490209050010

Baturin, G. N. (2011). Variations in the composition of the ferromanganese concretions of the Kara Sea. *Oceanology* 51, 148–156. doi: 10.1134/S0001437011010012

Baturin, G. N., and Dubinchuk, V. T. (2011). "The composition of ferromanganese nodules of the Chukchi and East Siberian Seas," in *Doklady earth sciences* (Dordrecht: Springer), 1258–1264.

Bau, M., Schmidt, K., Koschinsky, A., Hein, J., Kuhn, T., and Usui, A. (2014). Discriminating between different genetic types of marine ferro-manganese crusts and nodules based on rare earth elements and yttrium. *Chem. Geol.* 381, 1–9. doi: 10.1016/j.chemgeo.2014.05.004

Blöthe, M., Wegorzewski, A., Müller, C., Simon, F., Kuhn, T., and Schippers, A. (2015). Manganese-cycling microbial communities inside deep-sea manganese nodules. *Environ. Sci. Technol.* 49, 7692–7700. doi: 10.1021/es504930v

Bogdanov, Y. A., Gurvich, E. G., Bogdanova, O. Y., Ivanov, G. V., Isaeva, A. B., Muravév, K. G., et al. (1995). *Ferromanganese nodules of the kara sea*. 34, 722–732. (Moscow: Shirshov Institute of Oceanology (SIO RAS)).

Bonatti, E., Kraemer, T., and Rydell, H. (1972). *Ferromanganese deposits on the ocean floor* (Washington, D.C.: National Science Foundation (NSF)).

Borcard, D., Gillet, F., and Legendre, P. (2018). *Canonical ordination* (Cham: Springer). 203–297. doi: 10.1007/978-3-319-71404-2_6

Cui, Y., Liu, X., Liu, C., Gao, J., Fang, X., Liu, Y., et al. (2020). Mineralogy and geochemistry of ferromanganese oxide deposits from the Chukchi Sea in the Arctic Ocean. *Arctic Antarct. Alp. Res.* 52, 120–129. doi: 10.1080/15230430.2020.1738824

Eglinton, T. I., and Repeta, D. J. (2004). Marine organic geochemistry. . *Treatise geochemistry* 7, 145–180.

Ehrlich, H. L. (1999). Microbes as geological agents: their role in mineral formation. *Geomicrobiol. J.* 16, 135–153. doi: 10.1080/014904599270659

Folk, R. L., and Ward, W. C. (1957). Brazos River bar [Texas]; a study in the significance of grain size parameters. *J. Sediment. Res.* 27, 3–26. doi: 10.1306/74D70646-2B21-11D7-8648000102C1865D

Glasby, G. P., Emelyanov, E. M., Zhamoida, V. A., Baturin, G. N., Leipe, T., Bahlo, R., et al. (1997). Environments of formation of ferromanganese concretions in the Baltic Sea: A critical review. *Manganese Miner. Geochemistry Mineral. Terr. Mar. Depos.* 119, 213–237. doi: 10.1144/GSL.SP.1997.119.01.14

Grigoriev, A. G., Zhamoida, V. A., Gruzdov, K. A., and Krymsky, R. S. (2013). Age and growth rates of ferromanganese concretions from the gulf of Finland derived from 210Pb measurements. *Oceanology* 53, 345–351. doi: 10.1134/S0001437013030041

Hein, J. R., and Koschinsky, A. (2014). "Deep-ocean ferromanganese crusts and nodules," in *Treatise on geochemistry, 2nd ed.* (Amsterdam: Published by Elsevier Inc), 273–291. doi: 10.1016/B978-0-08-095975-7.01111-6

Ingri, J., and Pontér, C. (1987). Rare earth abundance patterns in ferromanganese concretions from the Gulf of Bothnia and the Barents Sea. *Geochim. Cosmochim. Acta* 51, 155–161.

Jiang, X.-D., Gong, J.-L., Ren, J.-B., Liu, Q.-S., Zhang, J., and Chou, Y.-M. (2020). An interdependent relationship between microbial ecosystems and ferromanganese nodules from the Western Pacific Ocean. *Sediment. Geol.* 398, 105588. doi: 10.1016/j.sedgeo.2019.105588

Karandashev, V. K., Turanov, A. N., Orlova, T. A., Lezhnev, A. E., Nosenko, S. V., Zolotareva, N. I., et al. (2008). Use of the inductively coupled plasma mass spectrometry for element analysis of environmental objects. *Inorg. Mater.* 44, 1491–1500. doi: 10.1134/S0020168508140045

Killops, S., and Killops, V. (2004). *Introduction to organic geochemistry* (Malden, MA USA: Blackwell Publishing Ltd). doi: 10.1002/9781118697214

Kolesnik, O. N., and Kolesnik, A. N. (2013). Specific chemical and mineral composition of ferromanganese nodules from the Chukchi Sea. *Russ. Geol. Geophys.* 54, 653–663. doi: 10.1016/j.rgg.2013.06.001

Kuhn, T., Wegorzewski, A., Rühlemann, C., and Vink, A. (2017). "Composition, formation, and occurrence of polymetallic nodules," in *Deep-sea mining* (Springer International Publishing, Cham), 23–63. doi: 10.1007/978-3-319-52557-0_2

Lai, M., Liu, Q., Wang, X., Sun, D., Ran, L., Li, X., et al. (2024). Heterogeneous marine environments diversify microbial-driven polymetallic nodule formation in the South China Sea. *Front. Mar. Sci.* 11. doi: 10.3389/fmars.2024.1430572

Lindh, M. V., Maillot, B. M., Shulse, C. N., Gooday, A. J., Amon, D. J., Smith, C. R., et al. (2017). From the surface to the deep-sea: bacterial distributions across polymetallic nodule fields in the clarion-clipperton zone of the pacific ocean. *Front. Microbiol.* 8. doi: 10.3389/fmicb.2017.01696

Majamäki, R., Wasiljeff, J., Purkamo, L., Hultman, J., Asmala, E., Yli-Hemminki, P., et al. (2025). Microbially enhanced growth and metal capture by ferromanganese concretions in a laboratory experiment. *Geobiology* 23 (1), e70010. doi: 10.1111/gbi.70010

Menendez, A., James, R., Shulga, N., Connelly, D., and Roberts, S. (2018). Linkages between the genesis and resource potential of ferromanganese deposits in the atlantic, pacific, and arctic oceans. *Minerals* 8, 197. doi: 10.3390/min8050197

Molari, M., Janssen, F., Vonnahme, T. R., Wenzhöfer, F., and Boetius, A. (2020). The contribution of microbial communities in polymetallic nodules to the diversity of the deep-sea microbiome of the Peru Basin, (4130–4198 m depth)*Biogeosciences* 17, 3203–3222. doi: 10.5194/bg-17-3203-2020

Potts, P. J., Tindle, A. G., and Webb, P. C. (1992). *Geochemical reference material compositions: rocks, minerals, sediments, soils, carbonates, refractories & ores used in research & industry* (London: Taylor & Francis).

Reykhard, L. Y., and Shulga, N. A. (2019). Fe-Mn nodule morphotypes from the NE Clarion-Clipperton Fracture Zone, Pacific Ocean: Comparison of mineralogy, geochemistry and genesis. *Ore Geol. Rev.* 110, 102933. doi: 10.1016/j.oregeorev.2019.102933

Rozanov, A. G. (2015). Redox system of the bottom sediments of the western Kara Sea. *Geochemistry Int.* 53, 987–1001. doi: 10.1134/S001670291511004X

Sattarova, V., Aksentov, K., Kirichenko, I., Yaroshchuk, E., Charkin, A., Zarubina, N., et al. (2025). Ferromanganese formations of the Chaunskaya Bay (East Siberian Sea): geochemistry and mineralogy. *Geo-Marine Lett.* 45, 23. doi: 10.1007/s00367-025-00813-9

Shi, L., Dong, H., Reguera, G., Beyenal, H., Lu, A., Liu, J., et al. (2016). Extracellular electron transfer mechanisms between microorganisms and minerals. *Nat. Rev. Microbiol.* 14, 651–662. doi: 10.1038/nrmicro.2016.93

Shiraishi, F., Mitsunobu, S., Suzuki, K., Hoshino, T., Morono, Y., and Inagaki, F. (2016). Dense microbial community on a ferromanganese nodule from the ultra-oligotrophic South Pacific Gyre: Implications for biogeochemical cycles. Earth Planet. *Sci. Lett.* 447, 10–20. doi: 10.1016/j.epsl.2016.04.021

Shulga, N. A. (2017). Distribution of n-alkanes in the ferromanganese nodule–sediment–pore water system (Clarion–Clipperton Fracture Zone). *Lithol. Miner. Resour.* 52, 435–441. doi: 10.1134/S0024490217060098

Shulga, N. A. (2018). Characteristics of alkanes in ferromanganese nodules of the clarion–clipperton fracture zone. *Oceanology* 58, 672–678. doi: 10.1134/S0001437018050156

Shulga, N., Abramov, S., Klyukina, A., Ryazantsev, K., and Gavrilov, S. (2022). Fast-growing Arctic Fe–Mn deposits from the Kara Sea as the refuges for cosmopolitan marine microorganisms. *Sci. Rep.* 12, 21967. doi: 10.1038/s41598-022-23449-6

Shulse, C. N., Maillot, B., Smith, C. R., and Church, M. J. (2017). Polymetallic nodules, sediments, and deep waters in the equatorial North Pacific exhibit highly diverse and distinct bacterial, archaeal, and microeukaryotic communities. *Microbiologyopen* 6, e00428. doi: 10.1002/mbo3.428

Team (2019). *RStudio: Integrated development for R* (Boston, MA: RStudio, Inc.). Available online at: https://www.rstudio.com (Accessed September 15, 2025).

Tully, B. J., and Heidelberg, J. F. (2013). Microbial communities associated with ferromanganese nodules and the surrounding sediments. *Front. Microbiol.* 4. doi: 10.3389/fmicb.2013.00161

Uurtio, V., Monteiro, J. M., Kandola, J., Shawe-Taylor, J., Fernandez-Reyes, D., and Rousu, J. (2018). A tutorial on canonical correlation methods. *ACM Comput. Surv.* 50, 1–33. doi: 10.1145/3136624

Vallius, H. (2007). (Ed.). *Holocene sedimentary environment and sediment geochemistry of the Eastern Gulf of Finland, Baltic Sea* (Espoo: Geological Survey of Finland).

Vereshchagin, O. S., Perova, E. N., Brusnitsyn, A. I., Ershova, V. B., Khudoley, A. K., Shilovskikh, V. V., et al. (2019). Ferro-manganese nodules from the Kara Sea: Mineralogy, geochemistry and genesis. *Ore Geol. Rev.* 106, 192–204. doi: 10.1016/j.oregeorev.2019.01.023

Wang, Y., Fang, X., Zhang, T., Li, Y., Wu, Y., He, D., et al. (2010). Predominance of even carbon-numbered n-alkanes from lacustrine sediments in Linxia Basin, NE Tibetan Plateau: Implications for climate change. *Appl. Geochemistry* 25, 1478–1486. doi: 10.1016/j.apgeochem.2010.07.002

Wang, X., Gan, L., Wiens, M., Schloßmacher, U., Schröder, H. C., and Müller, W. E. G. (2012). Distribution of microfossils within polymetallic nodules: biogenic clusters within manganese layers. *Mar. Biotechnol.* 14, 96–105. doi: 10.1007/s10126-011-9393-4

Wasiljeff, J., Salminen, J. M., Roberts, A. P., Hu, P., Brown, M., Kuva, J., et al. (2024). Morphology-dependent magnetic properties in shallow-water ferromanganese concretions. *Geochemistry Geophys. Geosystems* 25 (5), e2023GC011366. doi: 10.1029/2023GC011366

Wu, Y. H., Liao, L., Wang, C. S., Ma, W. L., Meng, F. X., Wu, M., et al. (2013). A comparison of microbial communities in deep-sea polymetallic nodules and the surrounding sediments in the Pacific Ocean. *Deep. Res. Part I Oceanogr. Res. Pap.* 79, 40–49. doi: 10.1016/j.dsr.2013.05.004

Yli-Hemminki, P., Jørgensen, K. S., and Lehtoranta, J. (2014). Iron–manganese concretions sustaining microbial life in the baltic sea: the structure of the bacterial community and enrichments in metal-oxidizing conditions. *Geomicrobiol. J.* 31, 263–275. doi: 10.1080/01490451.2013.819050

Zhamoida, V. A., Butylin, W. P., Glasby, G. P., and Popova, I. A. (1996). The nature of ferromanganese concretions from the eastern gulf of Finland, Baltic Sea. *Mar. Georesources Geotechnol.* 14, 161–176. doi: 10.1080/10641199609388309

Zhamoida, V., Grigoriev, A., Gruzdov, K., and Ryabchuk, D. (2007). The influence of ferromanganese concretions-forming processes in the eastern Gulf of Finland on the marine environment. *Geol. Surv. Finl. Spec. Pap.* 45, 21–32.

Zhang, F.-S., Lin, C.-Y., Bian, L.-Z., Glasby, G. P., and Zhamoida, V. A. (2002). Possible evidence for the biogenic formation of spheroidal ferromanganese concretions from the Eastern Gulf of Finland, the Baltic Sea. *Baltica* 15, 23–29.